J. Fluid Mech. (1975), *vol.* 69, *part* 4, *pp.* 803–823
Printed in Great Britain

Viscous shear flow past small bluff bodies attached to a plane wall

By MASARU KIYA AND MIKIO ARIE
Faculty of Engineering, Hokkaido University, Sapporo, Japan

(Received 18 September 1974)

Numerical solutions of the Navier–Stokes equations are presented for two-dimensional viscous flow past semicircular and semielliptical projections attached to a plane wall on which a laminar boundary layer has developed. Since the major axis is in the direction normal to the wall and is chosen to be twenty times as long as the minor axis in the present case, the flow around the semielliptical projection will approximately correspond to that around a normal flat plate. It is assumed that the height of each obstacle is so small in comparison with the local boundary-layer thickness that the approaching flow can be approximated by a uniform shear flow. Numerical solutions are obtained for the range 0·1–100 of the Reynolds number, which is defined in terms of the undisturbed approaching velocity at the top of the obstacle and its height. The geometrical shapes of the front and rear standing vortices, the drag coefficients and the pressure and shear-stress distributions are presented as functions of the Reynolds number. The computed results are discussed in connexion with the data already obtained in the other theoretical solutions and an experimental observation.

1. Introduction

An understanding of the flow around a bluff body attached to a plane wall is of practical importance in connexion with such diverse applications as the effect of a single roughness element on laminar boundary-layer transition or flow over an isolated hill or man-made structures on the ground. Most of these flows are three-dimensional and much too complicated to be accurately measured or theoretically analysed. Therefore, most of the investigations have been limited to two-dimensional cases, including normal or inclined flat plates (Good & Joubert 1968; Ranga Raju & Garde 1970), rectangular cylinders of various aspect ratios (Arie *et al.* 1975) and obstacles of the other shapes (Plate & Lin 1965; Kiya & Arie 1972), all being placed in turbulent boundary layers. Sedney (1973) has summarized the investigations of flow around small protuberances and their effects on boundary-layer flows.

Although most of the boundary layers of practical interest in which a body is immersed may be turbulent, the flow over a two-dimensional body in a laminar boundary layer is nevertheless important because of its association with the effects of a single two-dimensional roughness element on laminar boundary-layer transition, or the characteristics of the sublayer fence used to measure surface

shear stress. Furthermore, apart from these applications, this flow deserves attention in its own right as one of the fundamental problems in fluid dynamics. Tani & Sato (1956) and Klebanoff & Tidstrom (1972) reported measurements of velocity profiles around a two-dimensional isolated roughness element in the course of their studies of laminar boundary-layer transition due to a roughness element. Hunt (1971) considered theoretically the laminar far wake downstream of a cylindrical body on a plane wall, assuming that the height of the body was much smaller than the thickness of the boundary layer at the location of the body. The same kind of problem was considered by Smith (1973) by means of a different mathematical approach. Since their analyses employ a boundary-layer type of approximation, details of the flow around the body cannot be clarified by their methods.

Flow patterns around a body attached to a solid surface were obtained numerically by Dumitrescu, Cazacu & Craciun (1964) and Mills (1968) for the case of square-edged orifice plates installed respectively in a parallel-sided channel and a circular pipe by assuming a parabolic velocity profile for the approaching flow. Since the height of the orifice plate was taken to be 0·4 or 0·5 times the half-width of the channel or the radius of the pipe in their cases, the unbounded flow over a flat plate normal to a solid wall cannot be inferred from their solutions.

The present paper describes numerical solutions of the Navier–Stokes equations for flows over two typical shapes of bluff body, i.e. a semicircular projection and a normal flat plate. For the purpose of avoiding the computational uncertainties at the sharp edge of the plate, the normal flat plate is replaced by a thin oblate semielliptical projection with major axis normal to the wall. Also, the fluid flow is assumed to be steady and incompressible throughout this study.

2. Parameters to be considered

A two-dimensional body of height h is located at the bottom of a laminar boundary layer along a solid surface. The thickness of the boundary layer at the location of the body is denoted by δ. The velocity profile in the undisturbed boundary layer is generally a function of the two co-ordinates x and y, where the x axis is taken along the solid surface in the direction of flow and the y axis normal to the surface. However, when the body is sufficiently small, i.e.

$$h/\delta \ll 1, \tag{1}$$

the flow about the obstacle may be described in terms of simply the local velocity profile. More exactly, the length scale, say l, on which the wake behind the obstacle decays must be much smaller than that, say L, on which the boundary layer changes, i.e.

$$l/L \ll 1. \tag{2}$$

It is not easy to assess the order of magnitude of l/L in terms of h/δ and the appropriately defined Reynolds number of the obstacle for the entire range of laminar flows. It is evident, however, that (2) will hold if (1) is satisfied with a sufficient margin. Therefore, it may be assumed that with (1) satisfied the development of the boundary layer in the downstream direction may be neglected in the formulation of the flow around the obstacle.

The problem is now reduced to finding the flow about a body located on a plane wall with an approaching flow with velocity profile

$$v_{x\infty} = Uy/h, \quad v_{y\infty} = 0, \tag{3}$$

where v_x and v_y are the velocity components in the x and y directions and U is the velocity of the approaching flow at the top of the obstacle. The suffix ∞ refers to conditions far upstream of the obstacle. The flow about the obstacle in this situation is governed by the following four parameters: the shear velocity u_τ, the height h of the obstacle, the fluid density ρ and the kinematic viscosity of the fluid ν. The shear velocity is related to U by the equation

$$u_\tau^2 = \nu U/h. \tag{4}$$

Therefore, the properties of the flow about the obstacle can be completely described by the Reynolds number R_h defined by

$$R_h = Uh/\nu = (u_\tau h/\nu)^2. \tag{5}$$

There exists some knowledge concerning the relation between the height of a two-dimensional isolated roughness element and laminar boundary-layer transition. In the case of circular wires, the critical height h_1 which just does not affect transition can be represented by $u_\tau h_1/\nu = 7$. On the other hand, the minimum height h_2 for which transition occurs at the element itself is given by the relation (Schlichting 1968, p. 511) $u_\tau h_2/\nu = 15$ or 20. In the case of cupped cross-sections such as a semicircular projection, these values are considerably larger, whereas for sharp elements such as a normal flat plate they become smaller. In any case, laminar flow over obstacles may be treated as steady when the Reynolds number R_h is smaller than a few hundred. There is a practical application in this range of the Reynolds number. The height of the sublayer fence which was employed by Head & Rechenberg (1962) was $h = 0{\cdot}05$ mm and the maximum value of $u_\tau h/\nu$ was 5. In the experiment of Patel (1965), this value was in the range 4–8.

3. Fundamental equations

It is convenient to refer all lengths to h and all velocities to U. The velocity profile of the approaching flow thus becomes in dimensionless form

$$v_{x\infty} = y, \quad v_{y\infty} = 0. \tag{6}$$

In an orthogonal curvilinear co-ordinate system (ξ, η) with corresponding velocity components (u, v) as shown in figure 1, the equation of continuity now becomes

$$\partial(qu)/\partial\xi + \partial(qv)/\partial\eta = 0, \tag{7}$$

where q is defined by

$$q^2 = \left(\frac{\partial x}{\partial \xi}\right)^2 + \left(\frac{\partial y}{\partial \xi}\right)^2 = \left(\frac{\partial x}{\partial \eta}\right)^2 + \left(\frac{\partial y}{\partial \eta}\right)^2. \tag{8}$$

This equation is automatically satisfied by introducing the stream function in the usual way:

$$\partial\psi/\partial\eta = qu, \quad \partial\psi/\partial\xi = -qv. \tag{9}$$

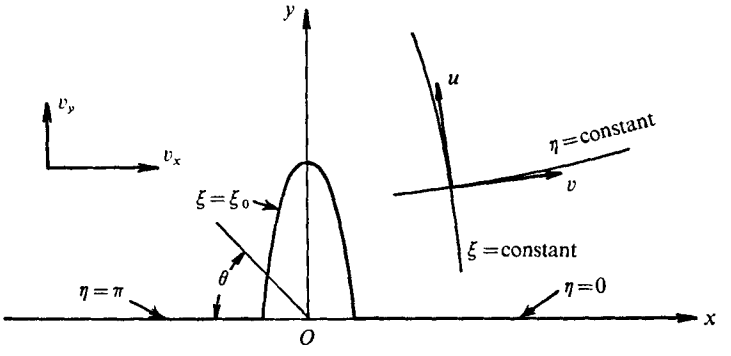

FIGURE 1. Co-ordinate system.

Then the scalar vorticity ζ be can be expressed as

$$\zeta = q^{-2}[\partial(qu)/\partial\eta - \partial(qv)/\partial\xi] = q^{-2}\Delta\psi, \tag{10}$$

where Δ is the Laplace operator $\partial^2/\partial\xi^2 + \partial^2/\partial\eta^2$. By eliminating the pressure terms from the Navier–Stokes equations, we have a vorticity transport equation of the form

$$\frac{\partial\psi}{\partial\eta}\frac{\partial\zeta}{\partial\xi} - \frac{\partial\psi}{\partial\xi}\frac{\partial\zeta}{\partial\eta} = \frac{1}{R_h}\Delta\zeta. \tag{11}$$

Since the cases of semicircular and semielliptical projections (hereafter simply called the semicircle and the semiellipse) are considered in the present paper, an appropriate co-ordinate system will be

$$x = f_i(\xi)\cos\eta, \quad y = g_i(\xi)\sin\eta, \tag{12a, b}$$

where $i = c$ (semicircle) or e (semiellipse). In what follows, the suffix c or e will be accompanied by other variables if necessary. f_i and g_i have the forms

$$f_c(\xi) = g_c(\xi) = e^{\xi}, \tag{13a}$$

$$f_e(\xi) = b_0\sinh\xi, \quad g_e(\xi) = b_0\cosh\xi, \tag{13b}$$

where b_0 is a positive constant. Then

$$q_c = e^{\xi}, \quad q_e = b_0(\cosh^2\xi - \sin^2\eta)^{\frac{1}{2}}. \tag{14a, b}$$

The surface of the obstacle corresponds to $\xi = \xi_0$, where

$$\xi_{0c} = 0 \quad \text{and} \quad \xi_{0e} = \operatorname{arccosh} b_0^{-1},$$

while the downstream side of the plane wall corresponds to $\eta = 0$ and the upstream side to $\eta = \pi$. The ratio λ of the lengths of the major and minor axes of the semiellipse is related to ξ_0 by

$$\lambda = (\tanh\xi_0)^{-1}. \tag{15}$$

The vanishing of the velocity on the solid surface requires the following boundary conditions:

$$q^{-1}\partial\psi/\partial\eta = q^{-1}\partial\psi/\partial\xi = 0 \quad \text{at} \quad \xi = \xi_0, \tag{16a}$$

$$q^{-1}\partial\psi/\partial\eta = q^{-1}\partial\psi/\partial\xi = 0 \quad \text{at} \quad \eta = 0, \tag{16b}$$

$$q^{-1}\partial\psi/\partial\eta = q^{-1}\partial\psi/\partial\xi = 0 \quad \text{at} \quad \eta = \pi. \tag{16c}$$

The other boundary conditions require that the velocity and vorticity at infinity should be equal to those of the uniform shear flow given by (6). In the numerical calculations, however, these conditions must be replaced by conditions at a finite distance from the obstacle. Here it may be convenient to use asymptotic solutions of the Navier–Stokes equations which are valid at large distances as the boundary conditions at infinity. This approach was adopted by Takami & Keller (1969) for viscous flow past a circular cylinder in a uniform stream by means of the asymptotic solution obtained by Imai (1951). An asymptotic solution in this category for uniform shear flow was reported by Hunt (1971). Since his solution contains a constant which is only approximately related to a component of the couple acting on the body, it is not easy to incorporate this solution into the boundary conditions at infinity. In this connexion it should be mentioned that Okajima, Takata & Asanuma (1971) examined the numerical solutions of Takami & Keller (1969) and those obtained by assuming that a uniform flow is coming in and going out at the outer boundary with the location of the boundary systematically changed. According to their conclusion, these two kinds of solutions will give approximately the same results for the flow in the vicinity of the cylinder as long as the distance from the cylinder to the outer boundary is more than a hundred times the radius of the cylinder. In view of this fact, therefore, the contour corresponding to $\xi = \xi_\infty$ is chosen as the boundary on which the condition of uniform shear flow is to be applied. ξ_∞ is a positive constant; its value will be discussed later. The boundary conditions at infinity are now replaced by

$$\psi = \tfrac{1}{2}y^2 = \tfrac{1}{2}g_i^2(\xi)\sin^2\eta, \quad \zeta = 1 \quad \text{at} \quad \xi = \xi_\infty. \tag{17a, b}$$

The curve $\xi = \xi_\infty$ is a semicircle of radius $\exp\xi_{\infty c}$ for the semicircular projection, while for the semielliptical projection it is the semiellipse

$$y = b_0\cosh\xi_{\infty e}[1-(x/b_0\sinh\xi_{\infty e})^2]^{\frac{1}{2}},$$

which is almost equivalent to a semicircle of radius $\frac{1}{2}\exp\xi_{\infty e}/\cosh\xi_{\infty e}$ for large values of $\xi_{\infty e}$.

The pressure distribution over the surface of the obstacle is calculated from

$$C_p(\xi_0,\eta) = C_p(\xi_0,\pi) + \frac{2}{R_h}\int_\eta^\pi \left[\frac{\partial\zeta}{\partial\xi}\right]_{\xi=\xi_0} d\eta, \tag{18}$$

where C_p is the pressure divided by $\frac{1}{2}\rho U^2$. The pressure drag coefficient C_{Dp}, which is the pressure drag divided by $\frac{1}{2}\rho U^2 h$, becomes

$$C_{Dp} = -\int_0^\pi C_p(\xi_0,\eta)\cos\eta\, d\eta. \tag{19}$$

The shear-stress coefficient C_τ, defined in the same manner, is given by

$$C_\tau(\xi_0,\eta) = -(2/R_h)\,\zeta(\xi_0,\eta) \tag{20}$$

on the surface of the obstacle. Thus the viscous drag coefficient C_{Ds} becomes

$$C_{Ds} = -\tanh\xi_0\int_0^\pi C_\tau(\xi_0,\eta)\sin\eta\, d\eta. \tag{21}$$

The total drag coefficient is

$$C_D = C_{Dp} + C_{Ds}. \tag{22}$$

Similarly, the moment coefficient of the obstacle C_M, which is defined as the moment divided by $\frac{1}{2}\rho U^2 h^2$, also consists of two components, i.e.

$$C_M = C_{Mp} + C_{Ms}, \tag{23}$$

where C_{Mp} is the part due to the pressure and C_{Ms} is that due to the surface shear stress. C_{Mp} and C_{Ms} can be calculated from

$$C_{Mp} = -\frac{1}{2\cosh^2 \xi_0} \int_0^\pi C_p(\xi_0, \eta) \sin 2\eta \, d\eta, \tag{24a}$$

$$C_{Ms} = -\tanh \xi_0 \int_0^\pi C_\tau(\xi_0, \eta) \, d\eta. \tag{24b}$$

4. Finite-difference procedure

Since the Reynolds numbers of interest in the present study are much larger than unity, the governing equations (10) and (11) with the boundary conditions (16) and (17) must be solved numerically by means of a finite-difference procedure. The nonlinear terms on the left-hand side of (11) are the main source of the numerical instability which has been encountered in the hitherto most widely used central difference schemes. Because of this instability, reliable numerical solutions of the steady Navier–Stokes equations have been computed by the central difference methods, for example, only for Reynolds numbers less than about 60 in the case of the flow around a circular cylinder in a uniform stream.

On the other hand the upwind-differencing scheme, which employs forward or downward differencing for the nonlinear terms according to the direction of the velocity vector, is known to provide increased calculational stability even in high Reynolds number flows. Most of the applications of this method have been to the calculation of internal flows, i.e. flows in pipes or in regions enclosed by solid boundaries. As far as the authors are aware, external flows which have been solved using upwind differencing are limited to the unsteady flow about a circular cylinder (Thoman & Szewczyk 1969) and that over a downward-facing step (Roache & Mueller 1970). The use of directional differencing as a remedy for numerical instability has been criticized because an artificial viscosity introduced by the numerical scheme results in only first-order accuracy. Good agreement, however, is found between the results of Thoman & Szewczyk and data from other numerical studies and experimental observations. Therefore this method was chosen in the present study as a compromise between accuracy and computer run time.

We divide the region of flow into rectangular cells with spacings k and l respectively in the ξ and η directions. Let the numbers of cells in the ξ and η directions be N_ξ and N_η. Then $k = (\xi_\infty - \xi_0)/N_\xi$ and $l = \pi/N_\eta$. The values of the various functions at the grid point $\{(i-1)k, (j-1)l\}$ are identified by (i,j), with i increasing in the $+\xi$ direction and j increasing in the $+\eta$ direction. i and j are

integers in the ranges $1 \leqslant i \leqslant N_\xi + 1$ and $1 \leqslant j \leqslant N_\eta + 1$. With this notation, the finite-difference form of (11) gives the vorticity ζ_P at a grid point $P(i,j)$ in terms of the vorticities and the stream functions at the neighbouring eight grid points, i.e. $N(i,j+1)$, $S(i,j-1)$, $E(i+1,j)$, $W(i-1,j)$, $NE(i+1,j+1)$, $SE(i+1,j-1)$, $NW(i-1,j+1)$ and $SW(i-1,j-1)$, as follows (Gosman *et al.* 1969):

$$\zeta_P = A_N\zeta_N + A_S\zeta_S + A_E\zeta_E + A_W\zeta_W, \tag{25}$$

where

$$A_i = a_i/(a_N + a_S + a_E + a_W) \quad (i = N, S, E, W),$$

$$a_i = \begin{cases} \dfrac{2}{R_h}\dfrac{k}{l} + \tfrac{1}{4}(c_i + |c_i|) & (i = N, S), \\ \dfrac{2}{R_h}\dfrac{l}{k} + \tfrac{1}{4}(c_i + |c_i|) & (i = E, W), \end{cases}$$

$$c_N = \psi_E - \psi_W + \psi_{NE} - \psi_{NW},$$

$$c_S = \psi_W - \psi_E + \psi_{SW} - \psi_{SE},$$

$$c_E = \psi_S - \psi_N + \psi_{SE} - \psi_{NE},$$

$$c_W = \psi_N - \psi_S + \psi_{NW} - \psi_{SW}.$$

Application of the central difference scheme to (10) yields

$$\psi_P = \frac{k^2l^2}{2(k^2+l^2)}\{k^{-2}(\psi_E + \psi_W) + l^{-2}(\psi_N + \psi_S) - q_P^2\zeta_P\}. \tag{26}$$

The boundary condition on the solid surface given by (16) can be written in finite-difference form as

$$\psi(1,j) = \psi(i,1) = \psi(i,N_\eta+1) = 0, \tag{27a}$$

$$\zeta(1,j) = \frac{2}{k^2\{q(1,j)\}^2}\psi(2,j), \quad \zeta(i,1) = \frac{2}{l^2\{q(i,1)\}^2}\psi(i,2), \tag{27b,c}$$

$$\zeta(i,N_\eta+1) = \frac{2}{l^2\{q(i,N_\eta+1)\}^2}\psi(i,N_\eta), \tag{27d}$$

where $i = 1, 2, \ldots, N_\xi + 1$ and $j = 1, 2, \ldots, N_\eta + 1$. Similarly the boundary condition (17) becomes

$$\psi(N_\xi+1,j) = \tfrac{1}{2}\{f_i(N_\xi k)\}^2\sin^2(j-1)l, \quad \zeta(N_\xi+1,j) = 1, \tag{28a,b}$$

where $j = 1, 2, \ldots, N_\eta + 1$.

In the iterative procedure used to solve (25) and (26), relaxation factors α and β were used to stabilize the computations. They were defined by

$$\zeta_P^{(n)} = (1-\alpha)\,\zeta_P^{(n-1)} + \alpha\zeta_P^{(n)*}, \quad \psi_P^{(n)} = (1-\beta)\,\psi_P^{(n-1)} + \beta\psi_P^{(n)*},$$

where the superscripts (n) and $(n-1)$ indicate the values at the nth and $(n-1)$th iterations, respectively, and an asterisk indicates the most recently corrected value.

5. Results and discussion

Numerical solutions for the flow over a semicircle and a semiellipse with $\lambda = 20$ were obtained for 24 different Reynolds numbers, ranging from 0·1 to 100. The distance between the centre of the obstacle and the outer boundary at which

the condition (28) was applied was taken to be a hundred times the height of the obstacle throughout the present study. This distance is judged to be appropriate in view of the findings of Okajima *et al.* (1971). Moreover, there are two facts supporting the use of a boundary with an even smaller radius than that in the case of a circular or elliptical cylinder in a uniform stream. First, the length of the rear standing vortices for a semicircle is shorter than that for a circular cylinder in a uniform flow when the Reynolds number is more than about 10, as will be seen in figure 8. For the purpose of comparing the two cases, the Reynolds number R_∞ for a circular cylinder in a uniform flow is defined in terms of the approaching velocity and its radius. Second, Hunt's analysis (1971) indicates that the perturbation velocity in the wake far downstream of a body placed at the bottom of a boundary layer decreases with the distance downstream in proportion to x^{-1} as opposed to $x^{-\frac{1}{2}}$ in the case of a cylindrical body in a uniform flow. These two facts imply that flow disturbances caused by a body at the bottom of a boundary layer decrease more rapidly than those caused by a body in a uniform flow. Thus, the use of a nearer outer boundary for the former case can be justified.

The number of grid points $N_\xi \times N_\eta$ for the semicircle was chosen as 50×60, 100×30 or 31×30, the third combination being used for Reynolds numbers smaller than unity. The calculated results are not very sensitive to the mesh size employed. The length of the rear standing vortex at $R_h = 100$, for example, is larger by about 34 % for the case 50×60 than for the case of 100×30. However, the separation and reattachment angles, the drag coefficients and the moment coefficients are comparatively insensitive to mesh size and differ by only 10 % at most. Since the combination 100×30 yields rather coarse rectangular cells in the η direction, the results for the combination 50×60 are believed to be more accurate. Moreover, the latter combination may be a standard one in the sense that a number of calculations of the flow past a circular cylinder in a uniform stream have been made in the neighbourhood of this combination. Thus the calculations for the semiellipse were performed using this combination for all Reynolds numbers.

The convergence of solutions was checked at every iteration for all the grid points and the iterations were terminated when the maximum relative errors of the successive iterations became less than 10^{-4}.

Figures 2(*a*) and (*b*) show the streamlines and the equi-vorticity lines of the flow fields around the semicircle and the semiellipse for $R_h = 40$. A small standing vortex is formed in front of the obstacle. The existence of this vortex was also confirmed by the numerical solutions of Mills (1968) for an orifice plate in a circular pipe and was experimentally observed by Dumitrescu *et al.* (1964) for an orifice plate in a parallel-sided channel. Figure 3 shows the velocity profiles around the semicircle for the case $R_h = 40$.

Figure 4 shows the maximum vorticity $|\zeta(\xi_{0c}, \eta)|_{\max}$ on the surface of the semicircle as a function of the Reynolds number. In the range $R_h > 2$, the maximum vorticity is seen to be proportional to $R_h^{\frac{1}{3}}$. Therefore, the maximum shear-stress coefficient $|C_\tau(\xi_{0c}, \eta)|_{\max}$ is proportional to $R_h^{-\frac{2}{3}}$. In this connexion, it may be noted that, according to laminar boundary-layer theory (Ting 1960), the vorticity in a laminar boundary layer along a body in a uniform shear flow is of

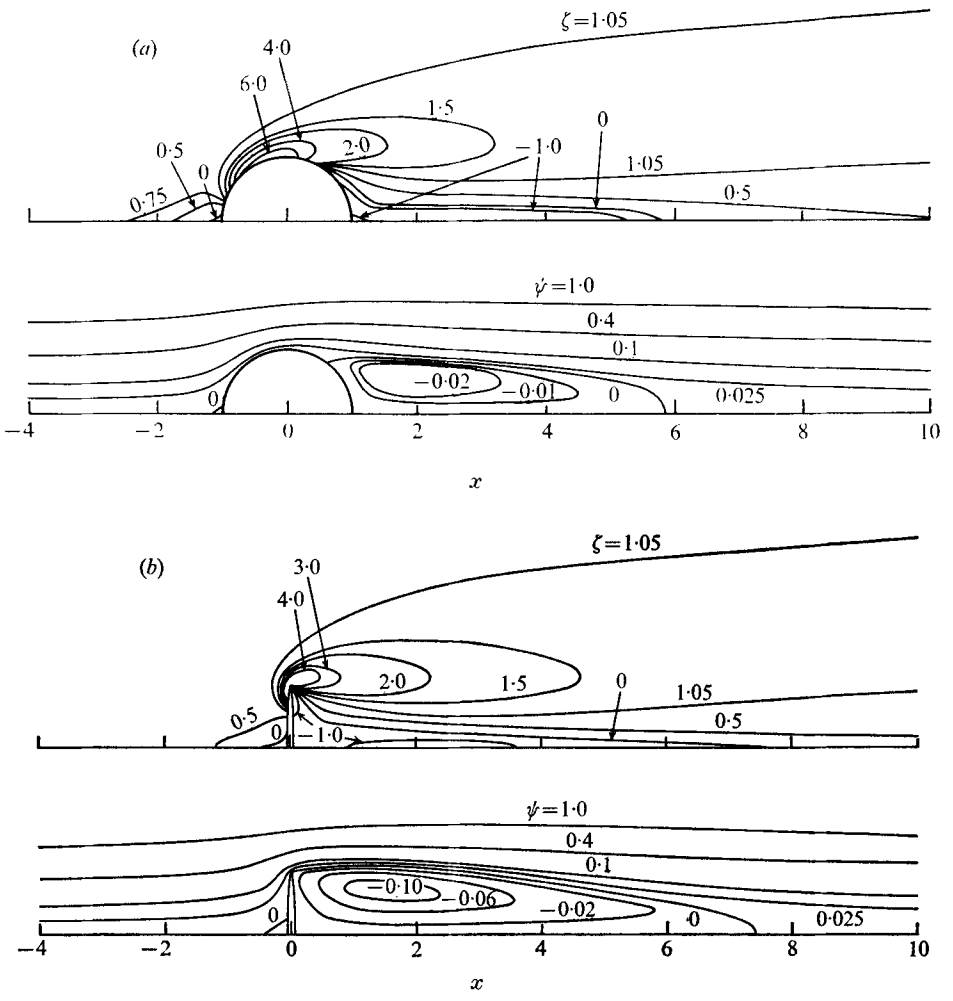

FIGURE 2. Streamlines and equi-vorticity lines around (*a*) the semicircular and (*b*) the semiellipticall projection for $R_h = 40$. $N_\xi = 50$, $N_\eta = 60$.

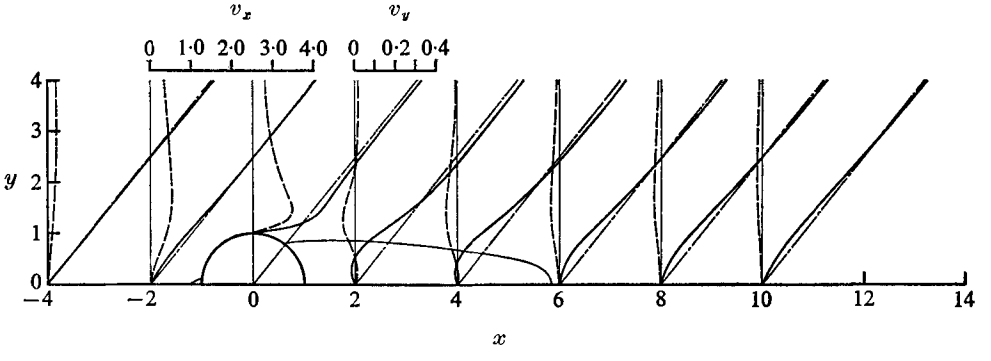

FIGURE 3. Velocity profiles around the semicircular projection for $R_h = 40$. $N_\xi = 50$, $N_\eta = 60$. ——, v_x; – – – –, v_y; — — —, undisturbed velocity profile.

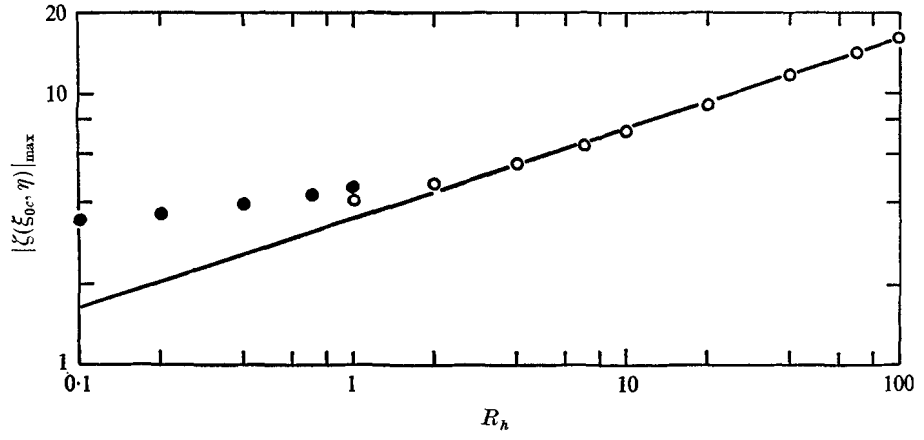

FIGURE 4. Maximum vorticity on the surface of the semicircular projection. ●, $N_\xi = 31$, $N_\eta = 30$; ○, $N_\xi = 50$, $N_\eta = 60$; ——, gradient = $\frac{1}{3}$.

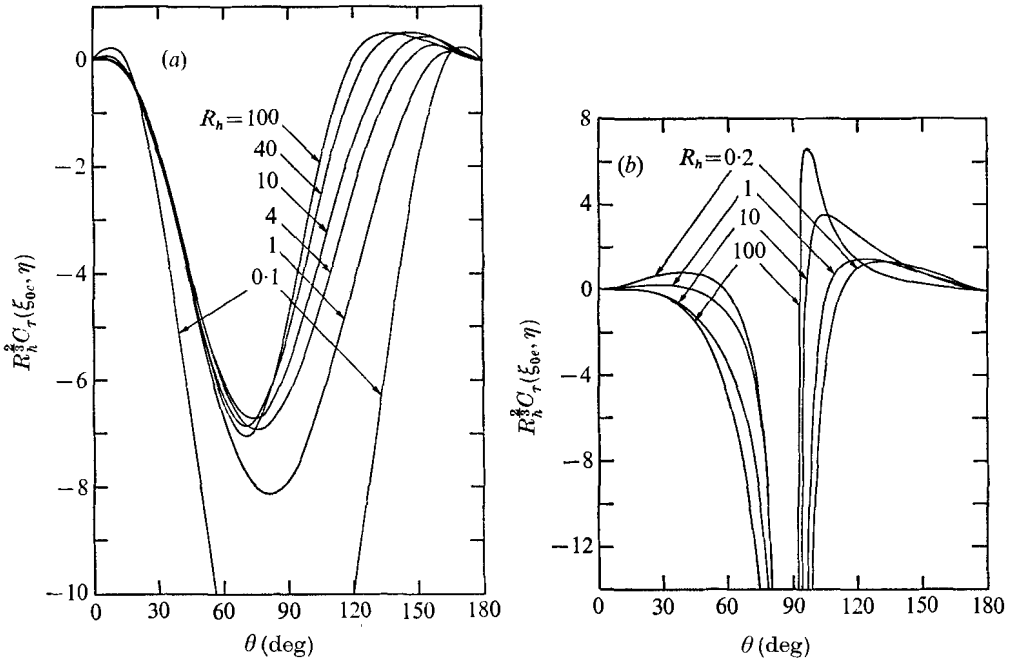

FIGURE 5. Distribution of shear stress on the surface of (*a*) the semicircular and (*b*) the semielliptical projection. $N_\xi = 50$, $N_\eta = 60$.

the order of the one-third power of the Reynolds number when the vorticity of the shear flow is relatively large. The Reynolds number in this case is defined in terms of the vorticity of the shear flow and a representative length of the body. This prediction is well confirmed by the numerical results presented in figure 4. The distribution of shear stress on the semicircle is shown in figure 5(*a*) in the form $R_h^{\frac{3}{2}} C_\tau(\xi_{0c}, \eta)$ for various Reynolds numbers. For higher Reynolds numbers,

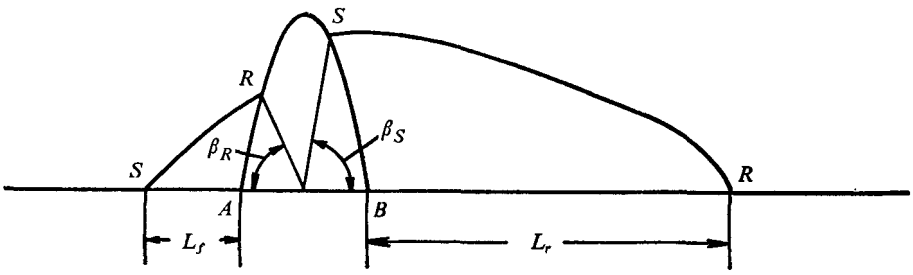

FIGURE 6. Definition sketch of standing vortices. S, separation point; R, reattachment point.

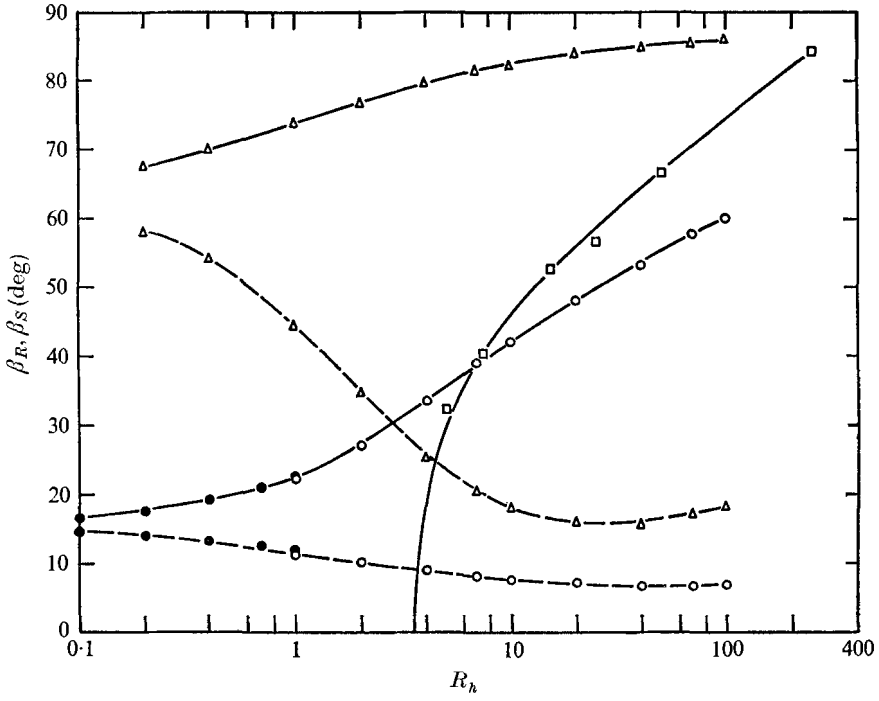

FIGURE 7. Variation of separation and reattachment angles with Reynolds number. ●, $N_\xi = 31, N_\eta = 30$, semicircular projection; ○, $N_\xi = 50, N_\eta = 60$, semicircular projection; △, $N_\xi = 50, N_\eta = 60$, semielliptical projection; □, circular cylinder in uniform flow (Hamielec & Raal 1969); ——, β_S; – – –, β_R.

$R_h^{\frac{2}{3}} C_\tau(\xi_{0c}, \eta)$ is clearly of order unity. Figure 5(*b*) shows the distribution of shear stress on the semiellipse. The steep gradient of the shear stress near the top of the semiellipse is caused by the large curvature there. In this case, the maximum vorticity does not follow the one-third power law mentioned above.

The points at which the shear stress on the obstacle changes its sign correspond to the reattachment or separation points. The definition sketch of the standing vortices is given in figure 6. The reattachment angle β_R and the separation angle β_S thus defined are shown in figure 7 as functions of the Reynolds number. Figure 8 shows the variation of the lengths L_f and L_r of the standing vortices with

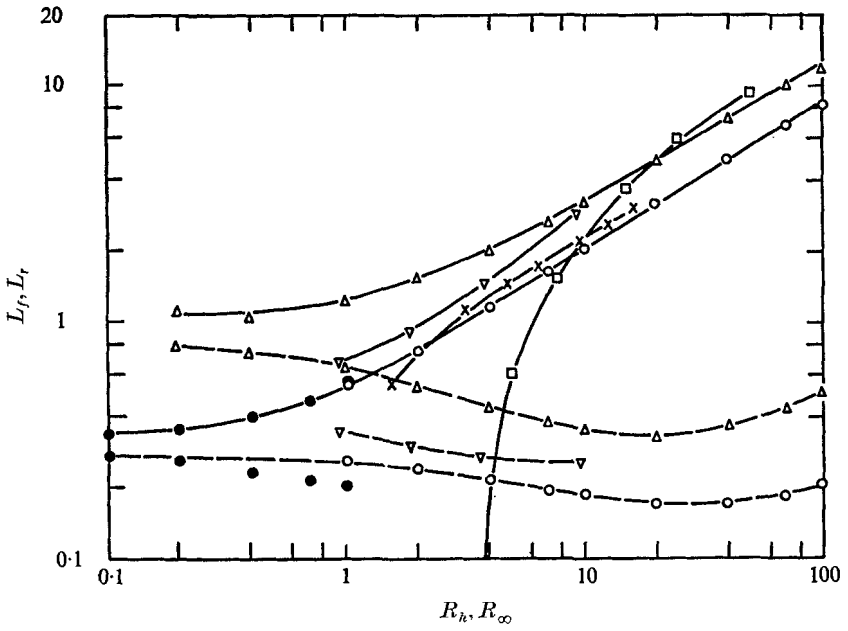

FIGURE 8. Variation of length of standing vortices with Reynolds number. ●, $N_\xi = 31$, $N_\eta = 30$, semicircular projection; ○, $N_\xi = 50$, $N_\eta = 60$, semicircular projection; △, $N_\xi = 50$, $N_\eta = 60$, semielliptical projection; ▽, orifice plate in circular pipe (Mills 1968); ×, orifice plate in parallel-sided channel (Dumitrescu *et al.* 1964); □, circular cylinder in uniform flow (Hamielec & Raal 1969); ——, L_r; – – – –, L_f.

the Reynolds number. In these figures, the separation angle and the length of the standing vortex for a circular cylinder in a uniform stream of infinite extent are shown for reference.

Standing vortices are found to exist even for a Reynolds number as small as 0·1. This situation is in contrast to the case of a circular cylinder in a uniform stream, in which a standing vortex appears behind the cylinder when R_∞ exceeds a value slightly less than 3·5. Although the creeping flow ($R_h = 0$) was not calculated in the present study, we obtained $L_{fc} = 0{\cdot}29$, $L_{rc} = 0{\cdot}30$, $\beta_{Rc} = 15{\cdot}6°$ and $\beta_{Sc} = 16{\cdot}0°$ at $R_h = 0{\cdot}01$ for the semicircle. This strongly suggests that standing vortices will exist upstream and downstream of the obstacle even in the limit $R_h \to 0$. In fact, Mills (1968) obtained standing vortices for creeping flow over a square-edged orifice plate in a circular pipe. Dumitrescu *et al.* (1964) computed the two-dimensional version of Mills' case for Reynolds numbers in the range $1{\cdot}60 \leqslant R_h \leqslant 12{\cdot}8$. Figure 2 of their paper, however, shows that the rear standing vortex vanishes when R_h becomes less than 0·64, which may certainly be erroneous. The standing vortices upstream and downstream of the obstacle become geometrically similar as the Reynolds number approaches zero, as may be seen from figures 7 and 8. This tendency is to be expected, because the solutions of the Navier–Stokes equations in the limit of zero Reynolds number yield flow patterns which remain unchanged even if the direction of flow is reversed. The standing vortices at $R_h = 0$ for the semicircle will have $L_{fc} = L_{rc} = 0{\cdot}295$ and

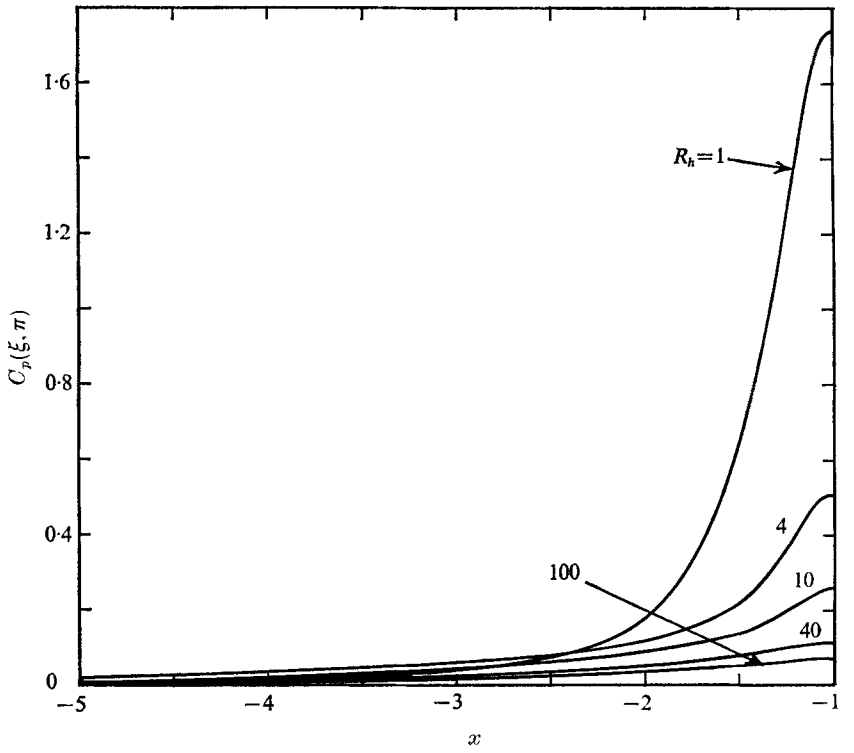

FIGURE 9. Pressure distribution on the plane wall upstream of the semicircular projection. $N_\xi = 50$, $N_\eta = 60$.

$\beta_{Rc} = \beta_{Sc} = 15{\cdot}8°$, as extrapolated from the data for $R_h = 0{\cdot}01$. At higher Reynolds numbers, on the other hand, the length of the rear standing vortex can be expressed by the formulae

$$L_{rc} = 0{\cdot}50R_h^{0{\cdot}61} \quad (2 < R_h < 100), \tag{29a}$$

$$L_{rc} = 0{\cdot}84R_h^{0{\cdot}60} \quad (7 < R_h < 100). \tag{29b}$$

Moreover, the separation angle and the length of the rear standing vortex for the semicircle are smaller than those for a circular cylinder in a uniform flow when the Reynolds number is more than about 10.

Figure 9 shows the pressure coefficient computed on the plane wall upstream of the semicircle, in which the static pressure on the wall at $x = -10$ is taken as the reference pressure. This choice of the reference pressure was made on the basis that the pressures near the outer boundary may be a little inaccurate because of the rather coarse mesh sizes there. Since the pressure gradient $[\partial C_p/\partial x]_{y=0}$ is almost zero at $x = -10$, there will be a negligible difference, if any, between the pressure distribution thus computed and that based on the pressure far upstream of the obstacle. The pressure coefficient C_{pf} at the front stagnation point A (see figure 6) is plotted in figure 10 as a function of the Reynolds number. The value of C_{pf} decreases monotonically as R_h increases with $C_{pfc} = 0{\cdot}115$ at $R_h = 40$ and $C_{pfc} = 0{\cdot}072$ at $R_h = 100$, whereas C_{pf} for a body in a uniform flow

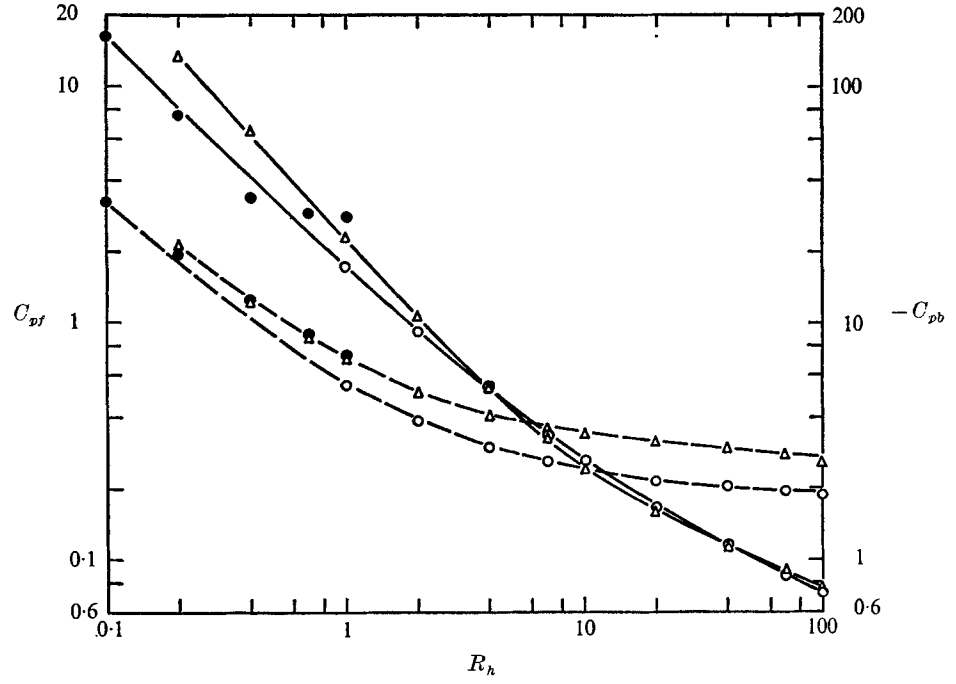

FIGURE 10. Variation of front and rear stagnation pressures with Reynolds number. ●, $N_\xi = 31, N_\eta = 30$, semicircular projection; ○, $N_\xi = 50, N_\eta = 60$, semicircular projection; △, $N_\xi = 50, N_\eta = 60$, semielliptical projection; ——, C_{pf}; – – – –, $-C_{pb}$.

approaches unity as the Reynolds number R_∞ increases. The $C_{pf} \sim R_h$ curves strongly suggest that C_{pf} will approach zero as R_h tends to infinity. This trend of the numerical results is supported by the fact that the stagnation pressure is everywhere zero for the inviscid shear flow described by (6), because the viscous flow upstream of the obstacle is understood to be approximated by the inviscid flow when the Reynolds number becomes very large. At higher Reynolds numbers, the value of C_{pf} becomes almost the same for the semicircle and the semiellipse, although their shapes are rather different. From this, it may be inferred that the $C_{pf} \sim R_h$ curve is little influenced by the shape of the bluff obstacle at Reynolds numbers higher than 5 or 6.

The pressure coefficient C_{pb} at the rear stagnation point B (see figure 6) is also included in figure 10. In contrast to C_{pf}, C_{pb} seems to approach a value which depends on the particular shape of the obstacle. As will physically be expected, $-C_{pb}$ is larger for the semiellipse than for the semicircle. Table 1 compares the value of $C_{pf} - C_{pb}$ for the semicircle with that for a circular cylinder in a uniform stream for a few Reynolds numbers. Notice that the former is larger than the latter.

Figures 11 (*a*) and (*b*) show the pressure coefficients for the semicircle and the semiellipse for various Reynolds numbers. At $R_h = 1$, 4 and 10 in figure 11 (*b*), the stagnation pressure at A is the lowest pressure on the front surface of the semiellipse. In contrast to this situation for the smaller Reynolds numbers, the stagnation pressure at A for $R_h = 40$ and 100 is the highest pressure on the front surface. The oddly different behaviour of the pressure for low and high

R_h or R_∞	$C_{pf}-C_{pb}$: Semicircular projection	$C_{pf}-C_{pb}$: Circular cylinder in uniform flow
1	7·196	4·368
10	2·647	1·798
20	2·338	1·653
100	1·956	1·53†

† Extrapolated value from the results of Takami & Keller (1969). Other data for the circular cylinder in a uniform flow are also from Takami & Keller (1969).

TABLE 1. Variation of $C_{pf}-C_{pb}$ with Reynolds number

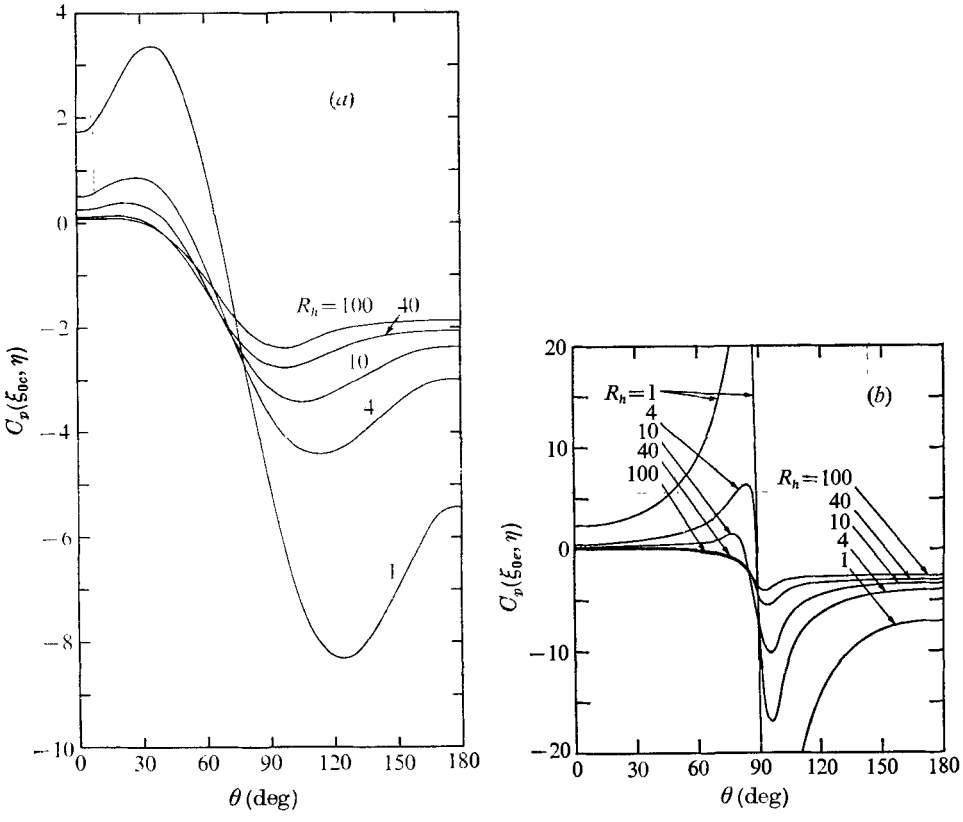

FIGURE 11. Pressure distribution on (*a*) the semicircular projection and (*b*) the semielliptical projection. $N_\xi = 50$, $N_\eta = 60$.

Reynolds numbers can be explained by the distribution of the equi-vorticity lines near the top of the semiellipse. The same behaviour of the pressure was found by Rimon (1969) for a thin oblate spheroid in a uniform stream, except that the front stagnation pressure approached unity as the Reynolds number increased. It is thus clear that this is caused by the large curvature near the top of the

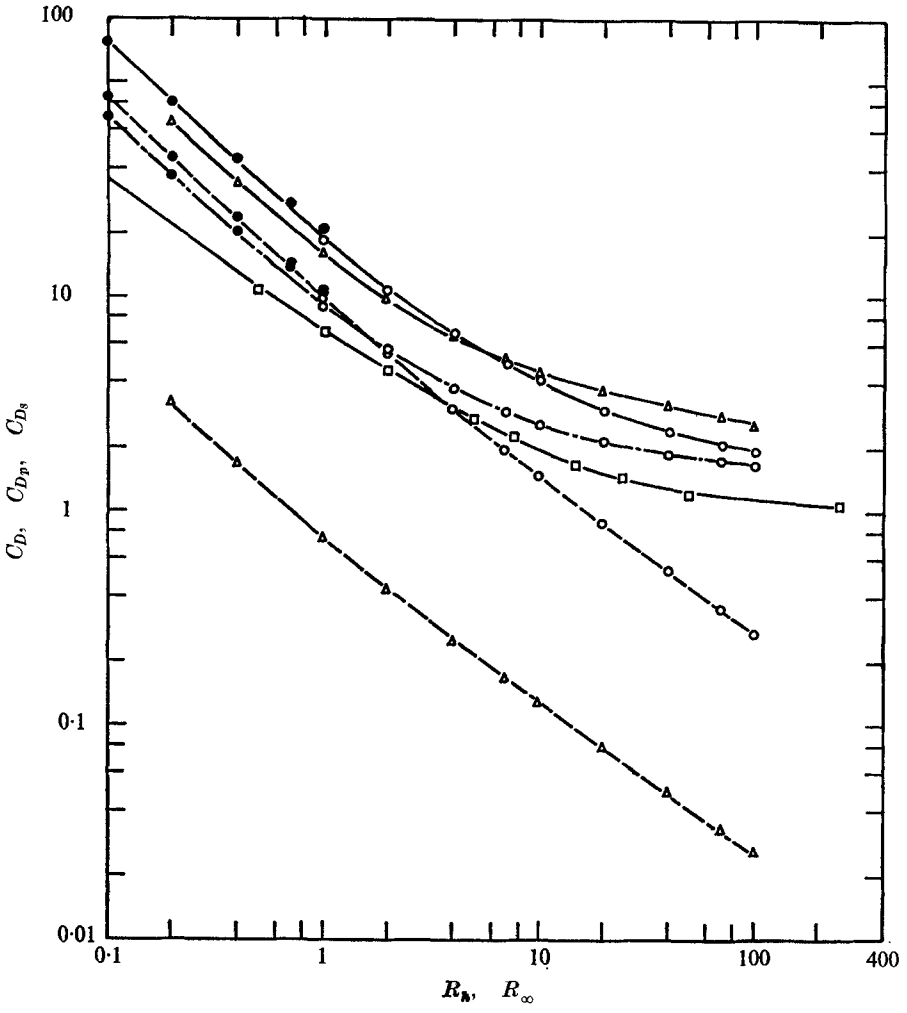

FIGURE 12. Variation of drag coefficients with Reynolds number. ●, $N_\xi = 31$, $N_\eta = 30$, semicircular projection; ○, $N_\xi = 50$, $N_\eta = 60$, semicircular projection; △, $N_\xi = 50$, $N_\eta = 60$, semielliptical projection; □, circular cylinder in uniform flow (Hamielec & Raal 1969); ——, C_D; – – – –, C_{D_s}; — — —, C_{D_p}.

semiellipse and is not in itself related to the existence of shear in the approaching flow. In the case of the semicircle, shown in figure 11(*a*), however, the pressure distribution on the surface is quite different from that on a circular cylinder in a uniform flow. The pressure coefficient at the front stagnation point A is the minimum pressure for all Reynolds numbers considered here for the former, while that for the latter is always the maximum pressure on the surface. This situation can also be explained by the distribution of the equi-vorticity lines near the surface of the semicircle.

Figure 12 shows the variation of the drag coefficient with the Reynolds number. The drag coefficient of a circular cylinder in a uniform flow is also included in this figure for reference. Most noteworthy is that the drag

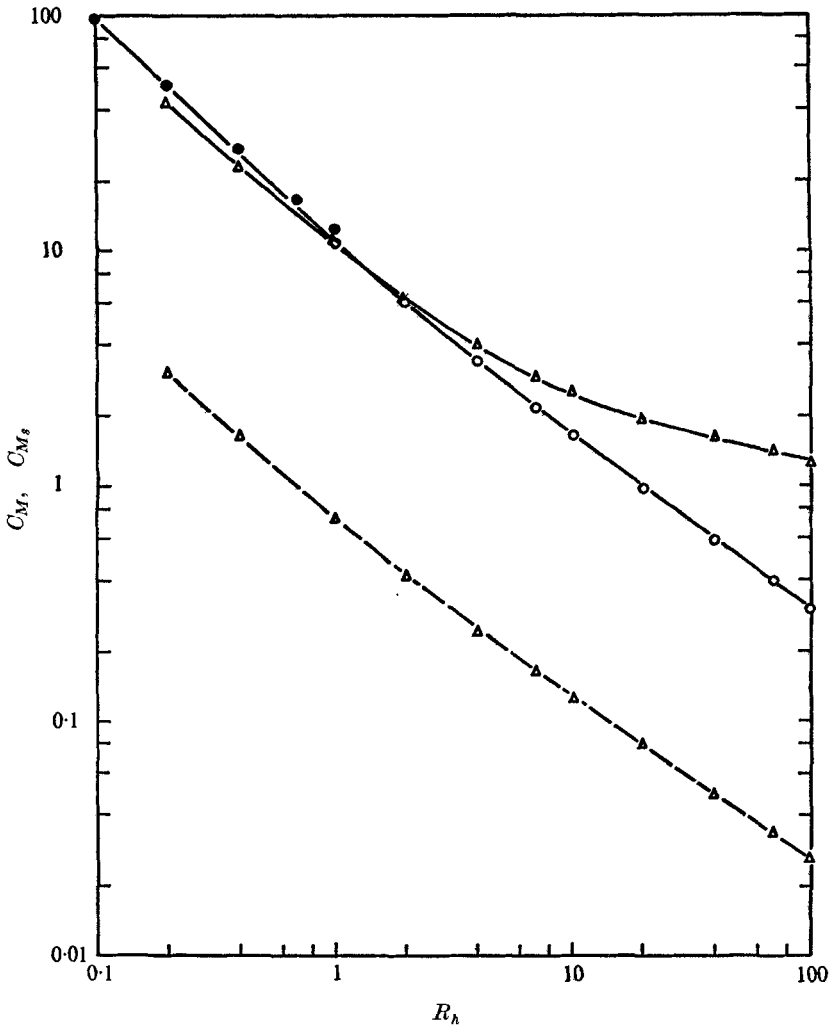

FIGURE 13. Variation of moment coefficients with Reynolds number. ●, $N_\xi = 31$, $N_\eta = 30$, semicircular projection; ○, $N_\xi = 50$, $N_\eta = 60$, semicircular projection; △, $N_\xi = 50$, $N_\eta = 60$, semielliptical projection; ——, C_M; – – – –, C_{M_s}.

coefficient of a semicircle is always larger than that of a circular cylinder in a uniform flow when R_h and R_∞ are the same. (Here, the drag coefficient of the latter is defined in the usual way as the drag force divided by $\frac{1}{2}\rho U^2(2h)$.) This fact can be explained by an increase in the vorticity on the semicircle proportional to the surface shear stress owing to the primary vorticity in the approaching stream. As shown in (18), the magnitude of the pressure on the semicircle is governed mainly by the vorticity gradient normal to the surface. The increased vorticity on the surface, in this case, leads to an increase in the vorticity gradient there. Accordingly, the pressure difference between the front and rear sides of the semicircle becomes larger than that for a circular cylinder in a uniform stream as has already been shown in table 1. The increased pressure difference and

surface shear stress yield the larger drag coefficient for the former case. Although the drag coefficient of a corresponding elliptical cylinder in a uniform stream is not known to the authors, it will certainly be smaller than that of the semiellipse considered here.

The contributions of the pressure and viscous drag coefficients to the total drag coefficient are approximately equal for the semicircle at Reynolds numbers less than about unity. This is also the case for a circular cylinder in a uniform flow. It may be added that the Oseen approximation of the Navier–Stokes equations yields exactly the same values of the pressure and viscous drag coefficients for this case, as shown by Tomotika & Aoi (1950). A solution in this category for an obstacle attached to a plane wall remains to be obtained.

The variation of the moment coefficient with Reynolds number is shown in figure 13. As previously mentioned, the moment coefficient is approximately related to the velocity profile in the far wake according to the theory of Hunt (1971). It was intended to examine Hunt's theory by comparing the computed velocity profile in the wake with that obtained theoretically. Since the mesh sizes become rather coarse in the far wake region, however, velocity profiles accurate enough to permit direct comparison with the theory could not be obtained.

Finally, the variation of the pressure difference Δp between the front and rear stagnation points, i.e. A and B in figure 6, with the shear stress $\tau_0 = \rho u_\tau^2$ will be considered. The relation between Δp and τ_0 written in the form

$$h^2\tau_0/(\rho\nu^2) = f\{h^2\Delta p/(\rho\nu^2)\}, \tag{30}$$

where all symbols denote dimensional quantities, has been used to determine τ_0 from the measurements of Δp. Here, the functional form of (30) depends on the particular shape of the obstacle. Figure 14 shows this relationship for the semicircle and the semiellipse, together with an analytical solution of Dean (1936) and the experimental results of Kimura (1974). Dean's analysis is concerned with creeping flow over a normal flat plate attached to a plane wall with an approaching velocity profile equivalent to (6). In this case, (30) becomes

$$h^2\Delta p/(\rho\nu^2) = 2{\cdot}90h^2\tau_0/(\rho\nu^2). \tag{31}$$

The computed curve for the semiellipse approximately tends to the straight line expressed by (31).

Kimura's measurements were performed using a normal fence of thickness 0·07 mm and span 16 mm placed at the bottom of a laminar boundary layer along a flat plate. The height of the fence was varied over the range 0·09–0·40 mm. Accordingly, it may be natural to expect the experimental data to fall in the region enclosed by the curves for the semicircle and the semiellipse. Although figure 14 shows that this expectation is approximately fulfilled, it should nevertheless be noted that the experimental data are nearer to the curve for the semicircle than to that for the semiellipse. There are three reasons for this situation. First, the shape of the fence is more like a rectangular cylinder rather than the semiellipse considered here. Second, it may be pointed out that the pressure holes upstream and downstream of the fence were of semicircular shape of radius 0·3 mm with centres at A and B (of figure 6), and are not considered to be small

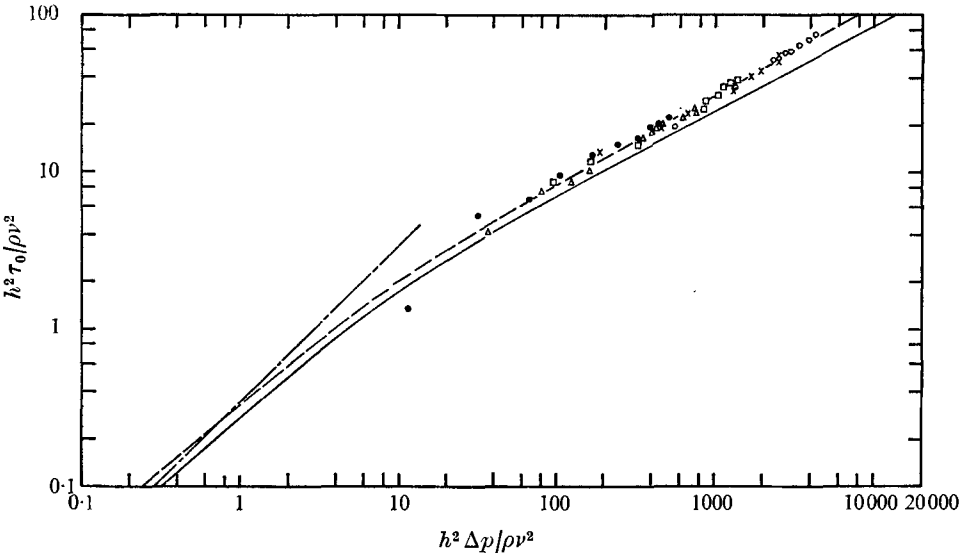

FIGURE 14. Pressure difference between front and rear stagnation points *vs.* shear stress on the plane wall. ----, $N_\xi = 50$, $N_\eta = 60$, semicircular projection; ——, $N_\xi = 50$, $N_\eta = 60$, semielliptical projection; ———, normal flat plate for creeping flow (Dean 1936). Experiment (Kimura 1974): ○, $h/b = 5{\cdot}7$; ×, $h/b = 4{\cdot}7$; □, $h/b = 3{\cdot}7$; △, $h/b = 3{\cdot}3$; ●, $h/b = 2{\cdot}9$; $b = 0{\cdot}07$ mm (thickness of plate), span = 16 mm.

enough compared with the height of the fence. Since the computed pressures on the plane wall change considerably in the vicinity of the obstacle, the relatively large pressure holes will measure an average pressure difference which is smaller than that between the pressures at the points A and B. Finally, the computations were performed for the completely two-dimensional case, whereas in the experiment the flow over the fence was only approximately two-dimensional. These three effects will yield a smaller pressure difference compared with the case where these were absent, if the value of τ_0 is the same. As shown in figure 14, the relation between the experimental data and the computed $\Delta p \sim \tau_0$ curve for the semiellipse confirms this tendency.

6. Conclusions

In the present study, numerical solutions have been obtained for viscous flow over two-dimensional obstacles of typical shapes, i.e. semicircular and semielliptical projections attached to a plane wall along which a laminar boundary layer has developed. Since the major axis of the semiellipse was taken to be twenty times as long as the minor axis and normal to the wall, the flow over the semiellipse approximately corresponded to that over a normal flat plate attached to the wall. It was assumed that the height of the obstacle was so small in comparison with the local boundary-layer thickness that the approaching flow could be approximated by a uniform shear flow. Numerical solutions in the range of Reynolds numbers $0{\cdot}1 \leqslant R_h \leqslant 100$ (R_h being defined in terms of the approaching

velocity at the top of the obstacle and its height h) were obtained by applying an upwind differencing scheme for the nonlinear terms of the vorticity transport equation.

The main results which have been obtained from this investigation are as follows.

(i) Standing vortices are formed both in front of and at the rear of the obstacle for all Reynolds numbers considered here. There is almost no doubt that these vortices will exist in the limit of zero Reynolds number. The length of the rear standing vortex can approximately be expressed as $0{\cdot}5hR_h^{0{\cdot}61}$ for the semicircle in the range $2 < R_h < 100$ and as $0{\cdot}84hR_h^{0{\cdot}60}$ for the semiellipse in the range $7 < R_h < 100$.

(ii) The pressure coefficient at one of the front stagnation points (point A in figure 6) approaches zero as the Reynolds number increases. For Reynolds numbers higher than about 10, the variation of the pressure coefficient with Reynolds number is rather insensitive to the particular shape of the obstacle.

(iii) The drag coefficient of the semicircle is larger than that of a circular cylinder in a uniform stream of infinite extent, for the same Reynolds number. Here the Reynolds number for a cylinder is defined in terms of the approaching velocity and its radius. This fact can be interpreted as an increase in the vorticity on the semicircle which is caused by the primary vorticity in the approaching shear flow.

(iv) The variation of the computed pressure difference between the front and rear stagnation points (points A and B in figure 6) with the undisturbed wall shear stress compares well with the analytical result for creeping flow in the range of smaller Reynolds numbers and with an experimental result in the range of higher Reynolds numbers.

(v) The maximum vorticity on the semicircle is proportional to $R_h^{\frac{1}{2}}$ for Reynolds numbers higher than about 4. This fact is consistent with the prediction of laminar boundary-layer theory for two-dimensional bodies in a uniform shear flow.

REFERENCES

Arie, M., Kiya, M., Tamura, H. & Kanayama, Y. 1975 On the flow over rectangular cylinders immersed in turbulent boundary layers. *Trans. J.S.M.E.* **41**, 839.

Dean, W. R. 1936 Note on the slow motion of fluid. *Proc. Camb. Phil. Soc.* **32**, 598.

Dumitrescu, D., Cazacu, M. D. & Craciun, C. I. 1964 Solutions numériques et recherches expérimentales dans l'hydrodynamique des fluides visqueux, à de nombres de Reynolds petits. *Proc. 11th. Int. Cong. Appl. Mech., Munich* (ed. H. Goertler), p. 1170.

Good, M. C. & Joubert, P. N. 1968 The form drag of two-dimensional bluff-plates immersed in turbulent boundary layers. *J. Fluid Mech.* **31**, 547.

Gosman, A. D., Pun, W. M., Runchal, A. K., Spalding, D. B. & Wolfshtein, M. 1969 *Heat and Mass Transfer in Recirculating Flows.* Academic Press.

Hamielec, A. E. & Raal, J. D. 1969 Numerical studies of viscous flow around circular cylinders. *Phys. Fluids*, **12**, 11.

Head, M. R. & Rechenberg, I. 1962 The Preston tube as means of measuring skin friction. *J. Fluid Mech.* **14**, 1.

Hunt, J. C. R. 1971 A theory for the laminar wake of a two-dimensional body in a boundary layer. *J. Fluid Mech.* **49**, 159.

IMAI, I. 1951 On the asymptotic behaviour of viscous fluid at a great distance from a cylindrical body, with special reference to Filon's paradox. *Proc. Roy. Soc.* A **208**, 487.

KIMURA, H. 1974 Study of sublayer fences. M.S. thesis, Faculty of Engineering, Hokkaido University.

KIYA, M. & ARIE, M. 1972 A free-streamline theory for bluff bodies attached to a plane wall. *J. Fluid Mech.* **56**, 201.

KLEBANOFF, P. S. & TIDSTROM, K. D. 1972 Mechanism by which a two-dimensional roughness element induces boundary-layer transition. *Phys. Fluids*, **15**, 1173.

MILLS, R. D. 1968 Numerical solutions of viscous flow through a pipe orifice at low Reynolds numbers. *J. Mech. Engng Sci.* **10**, 133.

OKAJIMA, A., TAKATA, H. & ASANUMA, T. 1971 Unsteady viscous flow around an oscillating aerofoil (1st Report, Numerical analysis, Part 1). *Trans. J.S.M.E.* **37**, 2300.

PATEL, V. C. 1965 Calibration of the Preston tube and limitations on its use in pressure *gradients. J. Fluid Mech.* **23**, 185.

PLATE, E. J. & LIN, C. W. 1965 The velocity field downstream from a two-dimensional model hill. Part 1. *Fluid Dyn. Diffusion Lab., Coll. Engng, Colorado State University, Final Rep. on Grant* DA AMC-36-039-63-G7, part 1.

RANGA RAJU, K. G. & GARDE, R. J. 1970 Resistance of an inclined plate placed on a plane boundary in two-dimensional flow. *Trans. A.S.M.E.* D **92**, 21.

RIMON, Y. 1969 Numerical solution of the incompressible time-dependent viscous flow past a thin oblate spheroid. *Phys. Fluids Suppl.* **12**, II-65.

ROACHE, P. J. & MUELLER, T. J. 1970 Numerical solutions of laminar separated flows. *A.I.A.A. J.* **8**, 530.

SCHLICHTING, H. 1968 *Boundary Layer Theory*, 6th edn. McGraw-Hill.

SEDNEY, R. 1973 A survey of the effects of small protuberances on boundary-layer flow. *A.I.A.A. J.* **11**, 782.

SMITH, F. T. 1973 Laminar flow over a small hump on a flat plate. *J. Fluid Mech.* **57**, 803.

TAKAMI, H. & KELLER, H. B. 1969 Steady two-dimensional viscous flow of an incompressible fluid past a circular cylinder. *Phys. Fluids Suppl.* **12**, II-51.

TANI, I. & SATO, H. 1956 Boundary-layer transition by roughness element. *J. Phys. Soc. Japan*, **11**, 1284.

THOMAN, D. C. & SZEWCZYK, A. A. 1969 Time-dependent viscous flow over a circular cylinder. *Phys. Fluids Suppl.* **12**, II-76.

TING, L. 1960 Boundary layer over a flat plate in presence of shear flow. *Phys. Fluids*, **3**, 78.

TOMOTIKA, S. & AOI, T. 1950 The steady flow of viscous fluid past a sphere and circular cylinder at small Reynolds numbers. *Quart. J. Mech. Appl. Math.* **3**, 140.